Hamilton Jesse I. (Orcid ID: 0000-0002-4463-481X)

Cardiac Cine Magnetic Resonance Fingerprinting (cine-MRF) for Combined Ejection Fraction, T_1, and T_2 Quantification

**Jesse I. Hamilton[1,2], Yun Jiang[1,3], Brendan Eck[2], Mark Griswold[2,3], and Nicole Seiberlich[1-3]

Author Affiliations:

[1]Department of Radiology, University of Michigan, Ann Arbor, MI, USA

[2]Department of Biomedical Engineering, Case Western Reserve University, Cleveland, OH, USA

[3]Department of Radiology, University Hospitals Cleveland Medical Center, Cleveland, OH, USA

Contact Email: JI Hamilton – hamiljes@med.umich.edu; Y Jiang – yunjiang@med.umich.edu; B Eck – ble14@case.edu; M Griswold – mag46@case.edu; N Seiberlich – nse@med.umich.edu

**Corresponding author at 1137 Catherine Street, Room 1590B, Ann Arbor, MI 48109

Running Head: Cardiac Cine Magnetic Resonance Fingerprinting

Word Count: 5753

Keywords: Magnetic Resonance Fingerprinting; myocardial tissue characterization; low-rank; ejection fraction; cine; T_1 mapping; T_2 mapping

Pages: 21

Figures: 12

This is the author manuscript accepted for publication and has undergone full peer review but has not been through the copyediting, typesetting, pagination and proofreading process, which may lead to differences between this version and the Version of Record. Please cite this article as doi: 10.1002/nbm.4323

Tables: 0

Supplementary Files: 7

Abstract

This study introduces a technique called cine Magnetic Resonance Fingerprinting (cine-MRF) for simultaneous T_1, T_2, and ejection fraction (EF) quantification. Data acquired with a free-running MRF sequence are retrospectively sorted into different cardiac phases using an external electrocardiogram signal. A low-rank reconstruction with a finite difference sparsity constraint along the cardiac motion dimension yields images resolved by cardiac phase. To improve SNR and precision in the parameter maps, these images are non-rigidly registered to the same phase and matched to a dictionary to generate T_1 and T_2 maps. Cine images for computing left ventricular volumes and EF are also derived from the same data. Cine-MRF was tested in simulations using a numerical relaxation phantom. Phantom and *in vivo* scans of 19 subjects were performed at 3T during a 10.9s breath-hold with an in-plane resolution of 1.6x1.6mm^2 and 24 cardiac phases. Left ventricular EF values obtained with cine-MRF agreed with the conventional cine images (mean bias -1.0%). Average myocardial T_1 times in diastole/systole were 1398/1391ms with cine-MRF, 1394/1378ms with ECG-triggered cMRF, and 1234/1212ms with MOLLI; and T_2 values were 30.7/30.3ms with cine-MRF, 32.6/32.9ms with ECG-triggered cMRF, and 37.6/41.0ms with T_2-prepared FLASH. Cine-MRF and ECG-triggered cMRF relaxation times were in good agreement. Cine-MRF T_1 values were significantly longer than MOLLI, and cine-MRF T_2 values were significantly shorter than T_2-prepared FLASH. In summary, cine-MRF can potentially streamline cardiac MRI exams by combining LV functional assessment and T_1/T_2 mapping into one time-efficient acquisition.

Keywords: Magnetic Resonance Fingerprinting; parameter mapping; low-rank; ejection fraction; cine

1. Introduction

Cardiac MRI is the gold standard for functional assessment of the left ventricle (LV) and is often employed for myocardial tissue characterization.[1] However, cardiac MRI exams can be time-consuming due to the large number of different scans that must be performed. Cine scans are an essential part of most protocols and provide information about cardiac function, including ejection fraction (EF), myocardial mass, and myocardial wall motion. Typically, a stack of 8-12 slices is acquired in short-axis view to cover the entire LV, with 1-2 slices imaged per breath-hold. Cardiac MRI protocols may also incorporate relaxation time mapping, which has gained interest recently. T_1 maps provide insight into inflammation,[2] fibrosis,[3] scar,[4,5] amyloid deposition,[6] and fatty infiltrative diseases,[7] while T_2 changes may be related to edema,[8,9] iron deposition,[10] or early transplant rejection.[11] Although faster mapping scans have been demonstrated,[12] in routine clinical practice native T_1 and T_2 maps may only be acquired over a few slices due to time constraints, with each map requiring a separate breath-held scan. LV functional assessment and relaxation time mapping taken together require several minutes of repeated breath-holds. These scans are tiring for patients, and failed breath-holds may lead to image artifacts or repeated scans.

Magnetic Resonance Fingerprinting (MRF) methods have been proposed for rapid and simultaneous quantification of T_1 and T_2 in multiple organs,[13–15] including the heart.[16] Cardiac MRF (cMRF) uses a time-varying pulse sequence to encode T_1 and T_2 information in the MRI signal timecourses. Data are collected using a highly undersampled spiral k-space trajectory. A dictionary of signal timecourses is generated using a Bloch equation simulation that models the net magnetization evolution. Then quantitative T_1 and T_2 maps are reconstructed by identifying

the dictionary entry that best matches the measured signal at each pixel. Because the scan is electrocardiogram (ECG) triggered, the cardiac rhythm alters the sequence timings and hence the shape of the cMRF signal evolutions, so a new dictionary is simulated after each acquisition to obtain accurate T_1 and T_2 estimates. In addition to heart rate, cMRF can compensate for other sources of measurement error by modeling these effects in the dictionary. Slice profile imperfections, preparation pulse efficiency, and B_1^+ inhomogeneities can be corrected in this way, potentially leading to more accurate and reproducible measurements.[17–19]

However, prospective ECG triggering is inefficient because data are only collected during part of the cardiac cycle. A single acquisition that combines relaxation time mapping with cine imaging to evaluate LV function would streamline the cardiac MRI exam workflow by reducing the total number of breathholds. Additionally, the cine images, T_1 maps, and T_2 maps would be inherently co-registered, which is not possible if these data are collected in separate acquisitions.

Recently, several novel techniques have been proposed for cardiac phase-resolved relaxation time mapping. Joint cine imaging and T_1 mapping techniques have been developed based on continuous Look-Locker acquisitions.[20–22] Methods that perform simultaneous T_1-T_2 mapping and cine imaging have also been demonstrated using continuous spoiled gradient echo readouts interrupted by inversions and T_2 preparation pulses. One such approach has been combined with golden angle radial k-space sampling and a low-rank patch-based (HD-PROST) reconstruction to achieve 3D coverage.[22,23] Another approach is CMR Multitasking, which uses a non-gated, free-breathing acquisition with a low-rank tensor reconstruction to achieve 2D phase-resolved T_1 and T_2 mapping.[24,25]

The goal of this study is to extend cMRF to a free-running and retrospectively gated acquisition called cine Magnetic Resonance Fingerprinting (cine-MRF). The main motivation is to improve efficiency by simultaneously obtaining co-registered T_1 and T_2 maps and cine images from one acquisition that has the same breathhold duration as a standard cine scan. A secondary goal is to achieve superior temporal resolution compared to prospectively ECG-triggered mapping sequences, including ECG-triggered cMRF, by using non-rigid image registration. Cine-MRF was evaluated in numerical simulations with a moving cardiac phantom, and it was compared with ECG-triggered cMRF and conventional sequences by scanning the ISMRM/NIST MRI system phantom and 19 healthy subjects at 3T.

2. Experimental

The following sections describe the different steps in the cine-MRF data processing workflow. Briefly, k-space data from a continuous MRF acquisition are retrospectively binned into different cardiac phases using an ECG signal. A low-rank reconstruction is performed that yields images in a low-dimensional subspace over multiple cardiac phases. These images are non-rigidly registered to the same target cardiac phase and matched to the dictionary to generate T_1 and T_2 maps. Contrast-weighted cine images are obtained from the same dataset for calculating ventricular volumes and ejection fraction (EF).

2.1 Pulse Sequence and Data Acquisition

In cine-MRF, data are acquired using a free-running sequence with variable flip angles, inversions, and T_2 preparations. The sequence uses a fast imaging with steady-state precession (FISP) readout because of its relative insensitivity to off-resonance.[26] The scan consists of 2060

repetition times (TRs) collected during a 10.9s breath-hold. The flip angle pattern is comprised of 20 half-sinusoids, referred to as "segments." Within each segment, the flip angles range from 4° to a maximum value no greater than 15°. A non-selective hyperbolic secant inversion is applied every five segments beginning with the first segment, or approximately every 2.7s, with an inversion time (TI) of 20.6ms. Non-selective T_2 preparation pulses with BIR-4 tip-down and tip-up pulses and an MLEV refocusing train[27] are applied every third, fourth, and fifth segments with variable echo times (TE_{T2prep}) between 30-80ms. The cine-MRF acquisition parameters are provided in Additional File 1.

Data are acquired using a variable density spiral k-space trajectory with minimum-time gradient design and 0^{th} moment compensation.[28] The spiral requires 24 interleaves to fully sample the central 25% of k-space and 48 interleaves to fully sample the periphery of k-space, and it has a readout duration of 3.3ms. The trajectory rotates by the golden angle every TR to produce spatially and temporally incoherent aliasing artifacts.[29]

2.2 Dictionary Simulation

The dictionary is constructed using a Bloch equation simulation with 500 spins and includes corrections for slice profile effects and preparation pulse efficiency.[17] All scans use a Hanning windowed sinc-shaped radiofrequency pulse with a time-bandwidth product of 2 and a duration of 0.8ms. A total of 13,925 signal evolutions are simulated for T_1 [10:10:2000 2050:50:3000]ms and T_2 [4:2:80 85:5:120 130:10:300]ms. Combinations where $T_1<T_2$ are excluded. The cine-MRF dictionary is only computed once because the sequence is free-running—the subject's cardiac rhythm affects how data are binned but does not change the sequence timings. This is in contrast to prospectively ECG-triggered cMRF, which requires scan-specific dictionary

generation because the cardiac rhythm influences the timings of each acquisition window. The cine-MRF dictionary occupies 200MB of memory and takes 4 minutes to simulate on a workstation with 12 CPU cores running parallelized MATLAB Mex code.

2.3 Low-Rank Reconstruction

The k-space readouts are retrospectively binned into different cardiac phases using the recorded ECG signal (Figure 1). Each RR interval is divided into 24 equally spaced phases, which is similar in number and temporal resolution to a conventional cine scan. The same number of readouts is not necessarily assigned to each phase due to variations in heart rate. On average, only 86 readouts (2060 TRs / 24 phases) are grouped into each phase. Thus, the data are highly undersampled considering that most MRF techniques employ sequence lengths of hundreds to thousands of TRs (note that the prior work with ECG-triggered cMRF used 768 TRs).[16]

Next, a low-rank reconstruction is performed to jointly reconstruct images at every cardiac phase that reside in a low-dimensional subspace derived from the dictionary (Figure 2). The reconstruction is reminiscent of XD-GRASP[30] and of low-rank methods that have been described for parameter mapping.[31–34] Let D denote the cine-MRF dictionary with size T (number of TRs) x P (number of T_1 and T_2 combinations). In this study, T=2060 and P=13,925. A low-rank approximation to the dictionary is found by computing the singular value decomposition (SVD) of the dictionary along the time dimension and only retaining the first K columns of the left singular matrix U corresponding to the K largest singular values, denoted by U_K.[35] The rank K is selected as the number of singular values that are larger than 3% of the first

singular value, which yields K=5 for this pulse sequence. A compressed dictionary D_K with size KxP is obtained by

$$D_K = U_K D \qquad (1)$$

The time series of undersampled cine-MRF images can also be projected to a set of images $\tilde{x}$ in the low-dimensional subspace, hereafter called "subspace images"

$$\tilde{x} = U_K x \qquad (2)$$

The low-rank reconstruction is formulated as an l_1-minimization problem

$$\min_{\tilde{x}} \left(\sum_{i=1}^{M} \left\| P_i (y - U_K^H F S \tilde{x}_i) \right\|_2^2 \right) + \lambda_1 \|\Psi_1 \tilde{x}\|_1 + \lambda_2 \|\Psi_2 \tilde{x}\|_1 \qquad (3)$$

In Equation (3), M=24 is the number of phases; $\tilde{x}_i$ denotes the subspace images for phase i and has size $N_y \times N_x \times K$, where N_y and N_x are the size of the x- and y-dimensions of the image; $\tilde{x}$ denotes the subspace images for all phases and has size $N_y \times N_x \times K \times M$; S denotes the coil sensitivity maps; F is the non-uniform fast Fourier Transform (NUFFT);[36] y is the acquired k-space data; and P_i is a sampling mask that extracts only those k-space readouts that fall within the temporal window of phase i.

Two sparsifying transforms are applied to the subspace images—Daubechies wavelets (Ψ_1) along the spatial dimensions and finite differences (Ψ_2) along the cardiac motion dimension. The regularization weights were chosen empirically by reconstructing several *in vivo* datasets with different λ_1 and λ_2 values and selecting parameters that visually yielded the best suppression of noise, reduction of spiral aliasing artifacts, and preservation of temporal dynamics (relative to the subspace images before the low-rank reconstruction). Figure 3 shows the effect of varying

the temporal finite difference penalty. All data shown in this work are reconstructed with λ_1=0.001 and λ_2=0.01 scaled relative to the maximum intensity in the subspace images. To estimate coil sensitivity maps, the subspace images that correspond to the first singular value are averaged over all cardiac phases before using the Walsh method.[37] Equation (3) is solved using nonlinear conjugate gradient descent with backtracking line search and a fixed 100 iterations,[38] and the resulting images are hereafter called "reconstructed subspace images."

2.4. Non-Rigid Registration and Pattern Matching

The reconstructed subspace images for each cardiac phase are non-rigidly registered to the same phase before performing pattern matching to improve the SNR and precision of the parameter maps. Deformation fields are computed using the reconstructed subspace images that correspond to the second singular value because they were empirically found to have high contrast between myocardium and blood. Deformation fields are calculated and saved between every possible pair of cardiac phases (e.g., phase 1→2, 1→3, ..., 24→22, 24→23). In total, there are 24x23=552 pairs of phases. This step is implemented in R using the open-source RNiftyReg software with a mutual information cost function.[39,40] Other parameters include a 3x3 final grid spacing, three multi-resolution levels, a maximum of 500 iterations per level, and 28 histogram intensity bins.

Next, a target phase is selected, and all the reconstructed subspace images are registered to the target phase using the deformation fields (Figure 4). For example, if phase 1 is chosen as the target phase, the reconstructed subspace images from phases 2 through 24 are spatially aligned to phase 1. After registration, the images are complex-averaged over the cardiac phase dimension to improve SNR. The complex-valued signal at each pixel in the registered subspace

images is compared to the compressed dictionary D_K using dot product matching to generate quantitative maps of T_1 and T_2 for phase 1. Image registration and pattern matching are repeated, each time choosing a different target phase, to construct T_1 and T_2 maps spatially aligned to every phase in the cardiac cycle. The use of image registration allows data from the entire scan to be used for pattern matching, thereby improving the SNR and precision of the parameter maps. The reconstructed subspace images that correspond to the second singular value are also used as cine images for evaluating LV function.

2.5 Numerical Simulations

Cine-MRF was investigated in two simulation experiments using the MRXCAT numerical cardiac phantom.[41] The phantom has 24 cardiac phases, modified to reflect relaxation times relevant for 3T MRI. Respiratory motion was not simulated since data are collected during a breath-hold. Motion states were assigned using an ECG recorded from an *in vivo* volunteer scan where the heart rate varied from 71-82bpm.

In the first experiment, the ground truth myocardial values were fixed at T_1=1410ms and T_2=50ms. Maps were reconstructed using three approaches. In the first approach, the low-rank reconstruction was performed without binning data into different cardiac phases. This is equivalent to solving Equation 3 with one cardiac phase and no temporal regularization (λ_2=0). In the second approach, data were binned into 24 phases and reconstructed using the low-rank method. However, the reconstructed subspace images for each cardiac phase (i.e., the images depicted in Figure 2B) were matched to the dictionary without image registration. In the third approach, the reconstructed subspace images were registered (as shown in Figure 4) so that all the collected data could be used for pattern matching. Accuracy was evaluated by measuring

the relative percent deviation from the ground truth T_1 and T_2 values in the myocardium. Precision was quantified using the coefficient of variation (CV), defined as the standard deviation in T_1 (or T_2) divided by the reference value in the myocardium. Image sharpness was evaluated by measuring the myocardial wall thickness. Line profiles were drawn across the septum in the T_1 and T_2 maps for every phase. Wall thickness was defined as the number of pixels along the profile having T_1 (or T_2) within 10% of the ground truth T_1 (1410ms) or T_2 (50ms) for myocardium.

The second experiment explored the performance of cine-MRF when the underlying tissue property values are changing. The ground truth myocardial T_1 and T_2 values were gradually swept from 1340ms and 50ms in diastole to 1400ms and 44ms in systole, respectively, and accuracy and precision were quantified as described above.

2.6 Phantom Experiments

The T_2 layer of the ISMRM/NIST MRI system phantom[42] was scanned at 3T (Siemens MAGNETOM Skyra, Erlangen, Germany) using an 18-channel cardiac array coil and 12 channels from the built-in spine array. A cine-MRF scan was acquired with 192x192 matrix, 300mm^2 FoV, 8mm slice thickness, and 1.6x1.6mm^2 resolution. Similar to the simulation experiments, 24 motion states were assigned using an ECG recorded during an *in vivo* scan, and maps were reconstructed using the proposed workflow. Since the phantom dataset has no motion, this experiment was intended to study the accuracy and precision in quantifying T_1 and T_2. The maps were analyzed by manually drawing regions of interest (ROIs) in each phantom sphere and measuring the mean and standard deviation in T_1 and T_2. Measurements were compared with reference values provided by NIST using Pearson's correlation and a Bland-

Altman analysis.[43] Consistency throughout the cardiac cycle was quantified by computing the CV of the mean T_1 and T_2 values over all phases.

2.7 In Vivo Volunteer Imaging

Nineteen subjects with no self-reported history of cardiovascular disease were enrolled in this IRB-approved, HIPAA-compliant study after obtaining written informed consent. Cardiac scans were performed in short-axis orientation at a medial slice position with breath-holds in end-expiration. Volume shimming centered on the LV was performed. All scans were acquired with 192x192 matrix, 300mm^2 FoV, 1.6x1.6mm^2 resolution, and 8mm slice thickness. In addition to cine-MRF, ECG-triggered cMRF scans were collected during a 16-heartbeat breath-hold with a 254ms scan window.[16] Two separate acquisitions were performed with both diastolic and systolic scan windows. Due to the duration of the longest T_2 preparation pulse, the minimum allowed trigger delay for the scan with the systolic scan window was 106ms. A new dictionary was simulated for each ECG-triggered cMRF scan using the recorded ECG timings and including the same T_1 and T_2 ranges as the cine-MRF dictionary. Maps were reconstructed using a low-rank reconstruction described in previous cMRF work,[32] which is equivalent to Eq. 3 with one cardiac phase and no temporal regularization (λ_2=0). Conventional T_1 and T_2 maps were acquired using Siemens MyoMaps.[44] The T_1 maps were collected using modified Look-Locker inversion recovery (MOLLI) with a 5(3)3 scheme (i.e., 5 imaging heartbeats, 3 recovery heartbeats, and 3 imaging heartbeats),[45] and T_2 maps were collected using T_2-prepared FLASH with a 1(3)1(3)1 scheme and echo times of 0, 25, and 55mms. All MyoMaps scans were repeated with diastolic and systolic scan windows. The MyoMaps scans used GRAPPA with an acceleration factor 2 and 24 autocalibration lines, 6/8 Partial Fourier, 35° flip angle, and a scan

window of 209ms. The maps were calculated inline at the scanner using curve fitting. A conventional cine scan with a balanced steady-state free precession (bSSFP) readout was acquired at a medial slice position with 24 phases, flip angle 35-70° (depending on the SAR limits), TR/TE 2.8/1.4ms, GRAPPA acceleration factor 2 with 24 autocalibration lines, and BW 965 Hz/pixel. Conventional cine scans were not acquired in two subjects due to time constraints. To evaluate the performance of cine-MRF for functional assessment over the entire LV, both standard bSSFP cine and cine-MRF scans were acquired in six subjects over multiple slices (one breathhold per slice). The number of slices in each short-axis stack ranged from 8 to 12 depending on the cardiac anatomy.

2.8 In Vivo Data Analysis

Maps were analyzed by manually drawing ROIs in six medial segments according to the standardized AHA model in diastolic and systolic phases, and the mean and standard deviation in T_1 and T_2 were measured for each segment.[46] For cine-MRF data, end-diastolic and end-systolic frames were identified as those with the largest and smallest blood pool volumes, respectively. The mean T_1 (and T_2) values in the septum were compared using a one-way ANOVA test with Tukey's posthoc correction with six groups, corresponding to the three techniques (cine-MRF, ECG-triggered cMRF, and MyoMaps) and two cardiac phases (diastole and systole). The septal T_1 and T_2 values between cine-MRF versus ECG-triggered cMRF and cine-MRF versus conventional mapping methods were also visualized using Bland-Altman plots. The intrasubject coefficient of variation (CV) was computed for each subject by dividing the standard deviation in T_1 (or T_2) by the mean value in a septal ROI to assess intrasubject variability. Then a one-way ANOVA test was performed using the same six groups as described

previously. A p-value below 0.05 was considered statistically significant. The intersubject CV was calculated by taking the standard deviation of the mean T_1 (or T_2) values measured for each subject and dividing by the group-averaged T_1 (or T_2). To assess intrareader repeatability, all T_1 and T_2 maps were contoured during a second session by the same reader, and the intraclass correlation coefficient (ICC) for each myocardial segment's mean T_1 and T_2 values was computed.

To assess LV function, the endocardial borders were manually contoured on one diastolic and one systolic frame of the cine datasets. Single-slice EF was quantified using

$$EF = \frac{EDV - ESV}{EDV} \times 100\% \quad (4)$$

where ESV and EDV are end-systolic volume and end-diastolic volume, respectively, excluding the papillary muscles. In the six datasets having whole LV coverage, EDV and ESV were computed for each slice and combined using Simpson's rule before calculating EF. Single-slice EF (17 out of 19 subjects) and whole-LV EDV, ESV, and EF measurements (6 out of 19 subjects) from cine-MRF and the standard cine scans were compared using a Bland-Altman analysis. To quantify the blood-myocardium contrast, the average signal within ROIs in the LV blood pool and septal myocardium was measured in each subject and used to calculate a blood-to-myocardium signal intensity ratio for the standard bSSFP cine images and MRF-derived cine images.

3. Results

3.1 Numerical Simulations

Results from the numerical simulations are shown in Figure 5. In these experiments, the ground truth T_1 and T_2 values were held fixed throughout the cardiac cycle. Maps reconstructed without cardiac phase binning (i.e., assuming a single cardiac phase although the heart was moving) had a relative error of 0.1% for T_1 and 3.2% for T_2, and a CV of 0.8% for T_1 and 3.0% for T_2. However, the maps suffered from motion artifacts and blurring, which is observed quantitatively in Figure 5B, where the myocardial wall thickness in the reconstructed maps (10 pixels) is larger than the thickness in the ground truth maps at diastole (8 pixels). After binning the data into 24 phases and using the low-rank reconstruction, the maps had improved accuracy for T_2 (relative error of 0.4% for T_1 and 0.5% for T_2) and slightly improved precision for T_2 (CV of 0.8% for T_1 and 2.3% for T_2). The measured wall thickness was consistent with the reference thickness. The combination of cardiac phase binning, low-rank reconstruction, and image registration yielded the best results in terms of accuracy (relative error of 0.2% for T_1 and 0.1% for T_2) and precision (CV of 0.4% for T_1 and 0.8% for T_2), and the measured wall thickness agreed with the reference thickness.

In the second simulation, the ground truth myocardial T_1 and T_2 values changed throughout the cardiac cycle. Figure 6 shows the mean and standard deviation in the measured relaxation times at different cardiac phases. The low-rank reconstruction without cardiac phase binning (i.e., assuming a single phase) yielded T_1 and T_2 values that are an average of the true diastolic and systolic relaxation times (1365.8ms for T_1 and 48.3ms for T_2). After binning the data into 24 phases and using the low-rank reconstruction, changes in T_1 and T_2 throughout the cardiac cycle were observed, although the longest T_1 and T_2 values were underestimated and the shortest T_1 and T_2 values were overestimated. The low-rank reconstruction followed by non-rigid

registration was not able to track the dynamics in T_1 and T_2 and instead yielded an average of the diastolic and systolic relaxation times. However, the maps had improved precision compared to the low-rank reconstruction without registration (see discussion above and precision measurements in Figure 5).

3.2 Phantom Experiments

Phantom validation was performed using the ISMRM/NIST MRI system phantom with motion states assigned to the data using an ECG recorded from a separate *in vivo* scan. Figure 7A shows the mean T_1 and T_2 measured within each phantom sphere over different phases. The cine-MRF relaxation times showed high consistency throughout the cardiac cycle (T_1 CV 0.30$\pm$0.26% and T_2 CV 0.76$\pm$0.81%). Figure 7B shows a linear regression comparing the reference T_1 and T_2 values provided by NIST with cine-MRF measurements that were averaged over all phases. A Bland-Altman plot of the same data is provided in Figure 7C. The mean bias for T_1 is 4.6ms with 95% limits of agreement (-29.8, 39.0)ms, and the mean bias for T_2 is -1.5ms with 95% limits of agreement (-11.1, 8.2)ms.

3.3 *In Vivo* Volunteer Imaging

Examples of T_1 and T_2 maps in diastole and systole for cine-MRF, ECG-triggered cMRF, and MyoMaps (MOLLI and T_2-prepared FLASH) are displayed in Figure 8A. Relaxation times measured in a septal ROI are provided on the insets. Note that it was not possible to capture the earliest part of systole using ECG-triggered cMRF and MyoMaps due to the long scan window (254ms for ECG-triggered cMRF and 209ms for MyoMaps), which may account for the different position of the myocardial wall. Figure 8B shows diastolic and systolic frames from the

cine images derived from cine-MRF and the conventional cine. Additional examples of cine-MRF T_1 and T_2 maps and cine images in movie format are provided in Supporting Videos 1-4.

Figure 9 summarizes the T_1 and T_2 values for each myocardial segment in diastole and systole averaged over all subjects. Over the entire myocardium in the medial slice, the average diastolic/systolic T_1 values were: cine-MRF 1397.7/1391.4ms, ECG-triggered cMRF 1394.4/1378.0ms, and MOLLI 1234.2/1212.1ms. The average diastolic/systolic T_2 times were: cine-MRF 30.7/30.3ms, ECG-triggered cMRF 32.6/32.9ms, and T_2-prepared FLASH 37.6/41.0ms. No significant differences were observed between cine-MRF and ECG-triggered cMRF T_1 and T_2 values, either in diastole or systole. The mean T_1 times measured with both cine-MRF and ECG-triggered cMRF were significantly higher than MOLLI in both diastolic and systolic phases ($p<0.01$). The mean T_2 values measured with cine-MRF and ECG-triggered cMRF were significantly lower than T_2-prepared FLASH in both diastole ($p<0.05$) and systole ($p<0.01$). No significant differences were observed between diastolic versus systolic relaxation times using cine-MRF or ECG-triggered cMRF. Mean T_2 times were significantly higher in systole compared to diastole using T_2-prepared FLASH ($p<0.05$). Bland-Altman plots comparing the mean T_1 and T_2 values acquired with cine-MRF, ECG-triggered cMRF, and conventional mapping sequences are shown in Figures 10 and 11.

For T_1, no significant differences in intrasubject CV were observed between methods or in diastolic versus systolic phases (Figure 12A). For T_2, no significant differences in intrasubject CV were seen between methods in diastole. For the systolic maps, the intrasubject CV for both cine-MRF and T_2-prepared FLASH were significantly higher than ECG-triggered cMRF ($p < 0.05$). As shown in Figure 12B, all techniques had a similar intersubject CV for T_1. For T_2, cine-

MRF had the highest intersubject variability (7.7% in diastole, 9.2% in systole), followed by ECG-triggered cMRF (6.4% in diastole, 8.7% in systole), and T_2-prepared FLASH had the lowest intersubject variability (5.3% in diastole, 6.5% in systole).

Graphs from the intrareader repeatability study are shown in Additional File 2. For T_1, the ICC for cine-MRF and ECG-triggered cMRF was above 0.9 for all segments, indicating excellent intrareader repeatability. For MOLLI, the ICC was above 0.9 for segments 7-9 and segment 12; however, the ICC was lower at 0.87 for segment 10 and 0.67 for segment 11. For T_2, all methods had ICC values above 0.9 for every segment, with the one exception being segment 11 for cine-MRF (ICC 0.87).

Figure 13 shows an example of contrast-weighted cine images from cine-MRF and the corresponding standard cine images in a healthy subject at multiple slice positions covering the left ventricle. Supporting Video 5 shows these datasets in movie format. When averaged over all subjects, the standard cine images had slightly higher CNR, with a blood-to-myocardium signal intensity ratio of 3.91 +/- 0.44 compared to 3.55 +/- 0.20 for the MRF-derived cine images. Figure 14 shows Bland-Altman plots of the LV functional measurements. For single-slice EF, good agreement was observed between the standard cine scan and cine-MRF with a mean bias of -0.3% and 95% limits of agreement (-3.4%, 2.7%). Over the entire LV, the mean bias in EF was -1.0% with 95% limits of agreement (-3.4%, 1.3%). For EDV, the mean bias was 2.2mL with 95% limits of agreement (-6.9mL, 11.3mL). For ESV, the mean bias was 1.9mL with 95% limits of agreement (-2.3mL, 6.2mL).

4. Discussion

The motivation behind this work was to streamline the typical cardiac MRI exam by combining LV functional assessment and T_1-T_2 mapping into a single acquisition. A novel technique called cine-MRF was introduced for simultaneously generating T_1 and T_2 maps and cine images for quantifying LV volumes and EF during a 10.9s breathhold per slice. This method achieves maps at 1.6x1.6mm^2 spatial resolution and 24 cardiac phases, which corresponds to a temporal resolution of 42ms per frame for a heart rate of 60bpm. Cine-MRF maps have a shorter effective acquisition window compared to other conventional cardiac mapping sequences, as well as compared to the original implementation of ECG-triggered cMRF with its 250ms acquisition window, which could reduce blurring and partial volume effects in the myocardium.

This work uses a low-rank reconstruction to recover subspace images at each cardiac phase. Similar to XD-GRASP, the reconstruction exploits correlations along the cardiac motion dimension using temporal finite differences.[30] The subspace images corresponding to the second singular value have an image contrast with bright blood and dark myocardium, similar to the standard bSSFP cine images. The CNR in the MRF-derived cine images is reduced relative to the standard cine images, as quantified by the blood-to-myocardium signal intensity ratio. Nevertheless, the LV volume and EF measurements derived from cine-MRF are in good agreement with those from the standard cine (Figure 14).

Prior work has explored the use of rigid registration for motion correction in brain MRF applications.[47–49] However, one novel aspect of this work is the use of non-rigid registration to align all the cine-MRF images to the same cardiac phase before pattern matching. This step is needed because there are only a few k-space readouts per phase after motion binning (on average, 86 TRs per phase). By using image registration, the entire signal evolution (i.e., all

2060 TRs) can be used for pattern matching to generate maps spatially aligned to the same cardiac phase. In addition, the non-rigid displacement fields may provide insight into wall motion abnormalities or myocardial strain, although this was beyond the scope of this study.

Another implementation of free-running cardiac MRF has also been proposed that uses a radial bSSFP MRF acquisition with a 29.4s breathhold duration. Maps over 8 cardiac phases are obtained using a low-rank tensor reconstruction.[50] One key difference is that the current study uses non-rigid image registration in order to use the entire MRF signal evolution for pattern matching. This enables a higher temporal resolution of 24 phases per cardiac cycle and a shorter breathhold duration of 10.9s.

Dictionary-based methods like MRF have the potential for reproducible T_1 and T_2 mapping because sources of measurement error can be modeled in the dictionary. The measurements obtained in this study are consistent with previously published values. This study obtained diastolic/systolic T_1 values of 1398/1391ms with cine-MRF, 1394/1378ms with ECG-triggered cMRF, and 1234/1212ms with MOLLI; and T_2 values of 30.7/30.3ms with cine-MRF, 32.6/32.9ms with ECG-triggered cMRF, and 37.6/41.0ms with T_2-prepared FLASH. Previous studies at 3T obtained average T_1 values of 1323-1340ms with ECG-triggered cMRF and 1227-1242ms with MOLLI, and average T_2 values of 34-38ms with ECG-triggered cMRF and 38ms with T_2-prepared FLASH.[17,32]

As shown in Figures 9-11, the T_1 values obtained using cine-MRF are higher than MOLLI, which has been reported previously for ECG-triggered cMRF.[32] One explanation for this difference is that slice profile imperfections and inversion pulse efficiency are modeled in the Bloch equation simulations when creating the MRF dictionaries, whereas MOLLI does not correct for these

factors. These corrections improve accuracy and cause myocardial T_1 to increase relative to uncorrected values.[17] The cine-MRF T_1 times are lower than values reported using SASHA (1477-1569ms at 3T), potentially because cine-MRF uses multiple inversion pulses and may be affected by magnetization transfer.[51,52]

Cine-MRF myocardial T_2 times tended to be lower than ECG-triggered cMRF, but this difference was not statistically significant. Both MRF scans did have significantly lower T_2 values than T_2-prepared FLASH, which has been observed before.[32] The causes for this difference are unclear. Studies in the brain have reported lower T_2 values using FISP-MRF compared to standard techniques.[18,53] Some explanations may include motion sensitivity along the unbalanced gradient direction (i.e., the slice axis),[26] diffusion weighting from the spoiler gradient,[54] intravoxel dephasing,[55] or magnetization transfer.[56]

One potential source of error not investigated in this study is through-plane motion. Through-plane motion has been shown to cause T_2 underestimation when using FISP-MRF in the brain, so it is likely that any through-plane motion during the cine-MRF scan may decrease the apparent T_2.[48] Movement of the myocardium in and out of the imaging slice will cause spins to experience an excitation history that is not reflected in the signal model and ultimately lead to inaccurate T_1 or T_2 measurements. This problem is not unique to cine-MRF and affects other free-running 2D tissue property mapping techniques. This study aims to minimize through-plane errors by using small flip angles for the excitation pulses (less than 15°) and non-selective inversion and T_2 preparation pulses. Data are collected during a breath-hold to avoid through-plane motion from respiration. Finally, a relatively large slice thickness (8mm) is used. Other slice orientations besides short-axis, such as long-axis, sagittal, or coronal, may reduce the

amount of through-plane motion caused by cardiac contraction. In the future, extending cine-MRF to a 3D free-breathing technique may circumvent issues related to through-plane motion and improve reproducibility.

Although cine-MRF yields T_1 and T_2 maps that depict the heart in diastolic or systolic phases, the simulation results in Figure 6 indicate that the relaxation times represent an average over the entire scan. This likely occurs because subspace images from all phases are registered to one target phase before pattern matching, which causes the estimated T_1 and T_2 values to reflect an average over the cardiac cycle. One potential solution to achieve true cardiac phase-resolved mapping while still maintaining high SNR is to combine motion correction with soft-weighted pattern matching. For example, when generating maps in the diastolic phase, less weight could be given to data acquired in systole, and vice versa.

There are several possibilities for future work. First, the pulse sequence used here was adapted from ECG-triggered cMRF and was not optimized for this application. Numerical optimization of the flip angles, TRs, or preparation pulses could reduce scan time, improve temporal resolution, or increase the sensitivity to T_1 and T_2. In particular, it may be inefficient to use T_2 preparation pulses in cine-MRF because they introduce pauses in data acquisition. Second, cardiac self-gating could be investigated to remove the need for an external ECG, either using the center of k-space,[22,57] image-based navigators,[58] or deep learning.[25] Third, the reconstruction time for cine-MRF is approximately 6 hours per dataset (330min for the low-rank reconstruction, 24min for non-rigid registration, and 3min for pattern matching). Parallel computing and GPU acceleration could make the reconstruction time feasible for clinical use. Fourth, the *in vivo* results are limited to native T_1 and T_2 mapping, and future work will evaluate the accuracy of

cine-MRF after injection of gadolinium contrast. Fifth, precision was quantified using the coefficient of variation, which can also decrease due to over-regularization in the low-rank reconstruction. It may be interesting to characterize cine-MRF using alternative measures of precision.[59] Sixth, cine-MRF will be applied in patient studies. This technique may be useful for patients with hypertrophic cardiomyopathy, where there is clinical value in measuring both EF and T_1 (and potentially T_2).[60] Another application may be imaging after exercise or pharmacological stress, where there is limited time to acquire data while subjects recover towards baseline. Finally, future work will study the feasibility of extending cine-MRF to a free-breathing acquisition for providing simultaneous cine, T_1, and T_2 maps covering the entire left ventricle using 3D k-space sampling or simultaneous multislice (SMS) imaging.[32,61]

5. Conclusions

In conclusion, a novel extension of Magnetic Resonance Fingerprinting, termed cine-MRF, is introduced for simultaneous T_1 and T_2 mapping and ejection fraction quantification. Cine-MRF employs non-rigid registration to align all the imaging data to the same cardiac phase before pattern matching, which improves the image quality and SNR of the T_1 and T_2 maps. Cine-MRF can potentially streamline the typical cardiac MRI exam workflow by combining functional assessment and relaxation time mapping into one time-efficient acquisition.

Conflicts of Interest

This work was funded by the SCMR Seed Grant, National Institutes of Health (NIH/NHLBI R01HL094557, NIH/NIDDK R01DK098503, NIH/NIBIB R01EB016728), National Science Foundation (NSF CBET 1553441), and Siemens Healthineers (Erlangen, Germany). The

funding sources were not involved in the study design; collection, analysis and interpretation of data; in the writing of the report; or in the decision to submit the article for publication.

Abbreviations

bSSFP	Balanced steady-state free precession
cMRF	Cardiac Magnetic Resonance Fingerprinting
ECG	Electrocardiogram
FISP	Fast imaging with steady-state precession
FLASH	Fast low angle shot
FoV	Field of view
MOLLI	Modified Look-Locker inversion recovery
MRF	Magnetic Resonance Fingerprinting
NUFFT	Non-uniform fast Fourier Transform
ROI	Region of interest
SVD	Singular value decomposition

References

1. Bogaert J, Dymarkowski S, Taylor AM, Muthurangu V. *Clinical Cardiac MRI*. 2nd ed. Springer-Verlag Berlin Heidelberg; 2012.
2. Hinojar R, Nagel E, Puntmann VO. T1 mapping in myocarditis - headway to a new era for cardiovascular magnetic resonance. *Expert Rev Cardiovasc Ther*. 2015;13(8):871-874.
3. Bull S, White SK, Piechnik SK, et al. Human non-contrast T1 values and correlation with histology in diffuse fibrosis. *Heart*. 2013;99(13):932-937.
4. Goldfarb JW, Arnold S, Han J. Recent myocardial infarction: assessment with unenhanced T1-weighted MR imaging. *Radiology*. 2007;245(1):245-250.
5. Okur A, Kantarcı M, Kızrak Y, et al. Quantitative evaluation of ischemic myocardial scar tissue by unenhanced T1 mapping using 3.0 Tesla MR scanner. *Diagn Interv Radiol*. 20(5):407-413.
6. Karamitsos TD, Piechnik SK, Banypersad SM, et al. Noncontrast T1 mapping for the diagnosis of cardiac amyloidosis. *JACC Cardiovasc Imaging*. 2013;6(4):488-497.
7. Sado DM, White SK, Piechnik SK, et al. Identification and assessment of anderson-fabry disease by cardiovascular magnetic resonance noncontrast myocardial T1 mapping. *Circ Cardiovasc Imaging*. 2013;6(3):392-398.
8. Giri S, Chung Y-C, Merchant A, et al. T2 quantification for improved detection of myocardial edema. *J Cardiovasc Magn Reson*. 2009;11(1):56.
9. Park CH, Choi E-Y, Kwon HM, et al. Quantitative T2 mapping for detecting myocardial edema after reperfusion of myocardial infarction: validation and comparison with T2-weighted images. *Int J Cardiovasc Imaging*. 2013;29 Suppl 1:65-72.
10. Anderson LJ, Holden S, Davis B, et al. Cardiovascular T2-star (T2*) magnetic resonance for the early diagnosis of myocardial iron overload. *Eur Heart J*. 2001;22(23):2171-2179.
11. Butler CR, Savu A, Bakal JA, et al. Correlation of cardiovascular magnetic resonance imaging findings and endomyocardial biopsy results in patients undergoing screening for heart transplant rejection. *J Heart Lung Transplant*. 2015;34(5):643-650.
12. Weingärtner S, Moeller S, Schmitter S, et al. Simultaneous multislice imaging for native myocardial T_1 mapping: Improved spatial coverage in a single breath-hold. *Magn Reson Med*. 2017;78(2):462-471.
13. Ma D, Gulani V, Seiberlich N, et al. Magnetic resonance fingerprinting. *Nature*. 2013;495(7440):187-192.
14. Chen Y, Jiang Y, Pahwa S, et al. MR Fingerprinting for Rapid Quantitative Abdominal Imaging. *Radiology*. 2016;279(1):278-286.
15. Rieger B, Akçakaya M, Pariente JC, et al. Time efficient whole-brain coverage with MR Fingerprinting using slice-interleaved echo-planar-imaging. *Sci Rep*. 2018;8(1):1-12.

16. Hamilton JI, Jiang Y, Chen Y, et al. MR fingerprinting for rapid quantification of myocardial T1, T2, and proton spin density. *Magn Reson Med*. 2017;77(4):1446-1458.

17. Hamilton JI, Jiang Y, Ma D, et al. Investigating and reducing the effects of confounding factors for robust T1 and T2 mapping with cardiac MR fingerprinting. *Magn Reson Imaging*. 2018;53:40-51.

18. Ma D, Coppo S, Chen Y, et al. Slice profile and B $_1$ corrections in 2D magnetic resonance fingerprinting. *Magn Reson Med*. 2017;78(5):1781-1789.

19. Buonincontri G, Schulte RF, Cosottini M, Tosetti M. Spiral MR fingerprinting at 7 T with simultaneous B1 estimation. *Magn Reson Imaging*. 2017;41:1-6.

20. Weingärtner S, Shenoy C, Rieger B, Schad LR, Schulz-Menger J, Akçakaya M. Temporally resolved parametric assessment of Z-magnetization recovery (TOPAZ): Dynamic myocardial T 1 mapping using a cine steady-state look-locker approach. *Magn Reson Med*. 2018;79(4):2087-2100.

21. Becker KM, Schulz-Menger J, Schaeffter T, Kolbitsch C. Simultaneous high-resolution cardiac T1 mapping and cine imaging using model-based iterative image reconstruction. *Magn Reson Med*. 2019;81(2):1080-1091.

22. Qi H, Jaubert O, Bustin A, et al. Free -running 3D w
with isotropic spatial resolution. *Magn Reson Med*. 2019;82(4):1331-1342.

23. Qi H, Bustin A, Cruz G, et al. Free-running simultaneous myocardial T1/T2 mapping and cine imaging with 3D whole-heart coverage and isotropic spatial resolution. *Magn Reson Imaging*. 2019;63:159-169.

24. Christodoulou AG, Shaw JL, Nguyen C, et al. Magnetic resonance multitasking for motion-resolved quantitative cardiovascular imaging. *Nat Biomed Eng*. 2018;2:215-226.

25. Shaw JL, Yang Q, Zhou Z, et al. Free -breathing, no
mapping with cardiovascular magnetic resonance multitasking. *Magn Reson Med*. 2019;81(4):2450-2463.

26. Jiang Y, Ma D, Seiberlich N, Gulani V, Griswold MA. MR fingerprinting using fast imaging with steady state precession (FISP) with spiral readout. *Magn Reson Med*. 2015;74(6):1621-1631.

27. Brittain JH, Hu BS, Wright GA, Meyer CH, Macovski A, Nishimura DG. Coronary angiography with magnetization-prepared T2 contrast. *Magn Reson Med*. 1995;33:689-696.

28. Hargreaves B. Variable-Density Spiral Design Functions. http://mrsrl.stanford.edu/~brian/vdspiral/. Published 2005. Accessed June 1, 2017.

29. Winkelmann S, Schaeffter T, Koehler T, Eggers H, Doessel O. An optimal radial profile order based on the Golden Ratio for time-resolved MRI. *IEEE Trans Med Imaging*. 2007;26(1):68-76.

30. Feng L, Axel L, Chandarana H, Block KT, Sodickson DK, Otazo R. XD-GRASP: Golden-

angle radial MRI with reconstruction of extra motion-state dimensions using compressed sensing. *Magn Reson Med*. 2016;75(2):775-788.

31. Assländer J, Cloos MA, Knoll F, Sodickson DK, Hennig J, Lattanzi R. Low rank alternating direction method of multipliers reconstruction for MR fingerprinting. *Magn Reson Med*. 2018;79(1):83-96.

32. Hamilton JI, Jiang Y, Ma D, et al. Simultaneous multislice cardiac magnetic resonance fingerprinting using low rank reconstruction. *NMR Biomed*. 2019;32(2):e4041.

33. Doneva M, Amthor T, Koken P, Sommer K, Börnert P. Matrix completion-based reconstruction for undersampled magnetic resonance fingerprinting data. *Magn Reson Imaging*. 2017;41:41-52.

34. Zhao B, Bilgic B, Adalsteinsson E, Griswold MA, Wald LL, Setsompop K. Simultaneous multislice magnetic resonance fingerprinting with low-rank and subspace modeling. In: *2017 39th Annual International Conference of the IEEE Engineering in Medicine and Biology Society (EMBC)*. Vol 2017. IEEE; 2017:3264-3268.

35. McGivney DF, Pierre E, Ma D, et al. SVD compression for magnetic resonance fingerprinting in the time domain. *IEEE Trans Med Imaging*. 2014;33(12):2311-2322.

36. Fessler J, Sutton B. Nonuniform fast Fourier transforms using min-max interpolation. *IEEE Trans Signal Process*. 2003;51(2):560-574.

37. Walsh D, Gmitro A, Marcellin M. Adaptive reconstruction of phased array MR imagery. *Magn Reson Med*. 2000;43(5):682-690.

38. Lustig M, Donoho D, Pauly JM. Sparse MRI: The application of compressed sensing for rapid MR imaging. *Magn Reson Med*. 2007;58(6):1182-1195.

39. Modat M, Ridgway GR, Taylor ZA, et al. Fast free-form deformation using graphics processing units. *Comput Methods Programs Biomed*. 2010;98(3):278-284.

40. Clayden J. CRAN- Package RNiftyReg. https://cran.r-project.org/package=RNiftyReg. Published 2019. Accessed June 24, 2019.

41. Wissmann L, Santelli C, Segars WP, Kozerke S. MRXCAT: Realistic numerical phantoms for cardiovascular magnetic resonance. *J Cardiovasc Magn Reson*. 2014;16(1):63.

42. Russek SE, Boss M, Jackson EF, et al. Characterization of NIST/ISMRM MRI System Phantom. In: *Proc. 20th Annu. Meet. ISMRM*. Melbourne, Australia; 2012:2456.

43. Bland JM, Altman DG. Statistical methods for assessing agreement between two methods of clinical measurement. *Lancet*. 1986;1(8476):307-310.

44. Siemens Medical Solutions USA. MyoMaps. https://usa.healthcare.siemens.com/magnetic-resonance-imaging/options-and-upgrades/clinical-applications/myomaps. Published 2018. Accessed February 27, 2018.

45. Messroghli DR, Radjenovic A, Kozerke S, Higgins DM, Sivananthan MU, Ridgway JP. Modified Look-Locker inversion recovery (MOLLI) for high-resolution T1 mapping of the

heart. *Magn Reson Med*. 2004;52(1):141-146.

46. Cerqueira MD. Standardized Myocardial Segmentation and Nomenclature for Tomographic Imaging of the Heart: A Statement for Healthcare Professionals From the Cardiac Imaging Committee of the Council on Clinical Cardiology of the American Heart Association. *Circulation*. 2002;105(4):539-542.
47. Mehta BB, Ma D, Pierre EY, Jiang Y, Coppo S, Griswold MA. Image reconstruction algorithm for motion insensitive MR Fingerprinting (MRF): MORF. *Magn Reson Med*. 2018;80(6):2485-2500.
48. Cruz G, Jaubert O, Schneider T, Botnar RM, Prieto C. Rigid motion-corrected magnetic resonance fingerprinting. *Magn Reson Med*. 2018;81(2):947-961.
49. Xu Z, Ye H, Lyu M, et al. Rigid motion correction for magnetic resonance fingerprinting with sliding-window reconstruction and image registration. *Magn Reson Imaging*. 2019;57:303-312.
50. Jaubert O, Cruz G, Bustin A, et al. Free-running cardiac magnetic resonance fingerprinting: Joint T1/T2 map and Cine imaging. *Magn Reson Imaging*. 2020;68:173-182.
51. Weingärtner S, Meßner NM, Budjan J, et al. Myocardial T1-mapping at 3T using saturation-recovery: reference values, precision and comparison with MOLLI. *J Cardiovasc Magn Reson*. 2016;18(1):84.
52. Robson MD, Piechnik SK, Tunnicliffe EM, Neubauer S. T1 measurements in the human myocardium: The effects of magnetization transfer on the SASHA and MOLLI sequences. *Magn Reson Med*. 2013;70(3):664-670.
53. Ma D, Jiang Y, Chen Y, et al. Fast 3D magnetic resonance fingerprinting for a whole-brain coverage. *Magn Reson Med*. 2018;79(4):2190-2197.
54. Kobayashi Y, Terada Y. Diffusion-weighting Caused by Spoiler Gradients in the Fast Imaging with Steady-state Precession Sequence May Lead to Inaccurate T2 Measurements in MR Fingerprinting. *Magn Reson Med Sci*. 2019;18(1):96-104.
55. Assländer J, Glaser SJ, Hennig J. Pseudo Steady-State Free Precession for MR-Fingerprinting. *Magn Reson Med*. 2017;77(3):1151-1161.
56. Gloor M, Scheffler K, Bieri O. Quantitative magnetization transfer imaging using balanced SSFP. *Magn Reson Med*. 2008;60(3):691-700.
57. Zhou R, Yang Y, Mathew RC, et al. Free-breathing cine imaging with motion-corrected reconstruction at 3T using SPiral Acquisition with Respiratory correction and Cardiac Self-gating (SPARCS). *Magn Reson Med*. 2019;82(2):706-720.
58. Larson AC, White RD, Laub G, McVeigh ER, Li D, Simonetti OP. Self-gated cardiac cine MRI. *Magn Reson Med*. 2004;51(1):93-102.
59. Roujol S, Weingärtner S, Foppa M, et al. Accuracy, Precision, and Reproducibility of Four T1 Mapping Sequences: A Head-to-Head Comparison of MOLLI, ShMOLLI, SASHA, and

SAPPHIRE. *Radiology*. 2014;272(3):683-689.

60. Dass S, Suttie JJ, Piechnik SK, et al. Myocardial tissue characterization using magnetic resonance noncontrast T1 mapping in hypertrophic and dilated cardiomyopathy. *Circ Cardiovasc Imaging*. 2012;5(6):726-733.

61. Barth M, Breuer F, Koopmans PJ, Norris DG, Poser BA. Simultaneous multislice (SMS) imaging techniques. *Magn Reson Med*. 2015;75(1):63-81.

Figure Captions

Figure 1. *Cardiac phase binning*. (A) The MRF spiral k-space readouts are retrospectively binned into different cardiac phases using an external ECG signal. Each RR interval is divided into 24 equally spaced bins, although only 3 are shown for clarity. Cine-MRF signal evolutions representative of myocardium (T_1=1400ms/T_2=50ms) and blood (T_1=2000ms/T_2=300ms) are also plotted. (B) A low-dimensional subspace is computed from the SVD of the MRF dictionary. The binned k-space data are projected onto this subspace and gridded to the image domain using the NUFFT. This work compresses the dictionary to rank 5, although only the first three (K=1 through K=3) subspace images are shown for clarity.

Figure 2. *Low-rank reconstruction*. Subspace images are shown for several different cardiac phases (A) before and (B) after performing the low-rank reconstruction. For clarity, only three subspace images for four cardiac phases are shown. The low-rank reconstruction reduces the appearance of spiral undersampling artifacts.

Figure 3. *Choice of temporal finite difference penalty in the low-rank reconstruction.* (A) Reconstructed subspace images are shown corresponding to the second singular value (K=2) in diastole and systole. The temporal finite difference penalty (λ_2) is varied from 0 to 0.05, scaled relative to the maximum image intensity, and the spatial Wavelet penalty is fixed at λ_1=0.001. When the temporal regularization penalty is too low (λ_2=0 and λ_2=0.001), the images

are corrupted by residual artifacts and noise enhancement. However, when the regularization penalty is too large (λ_2=0.05), there is temporal blurring along the cardiac motion dimension. A value of λ_2=0.01 is used for all datasets in this work and provides a tradeoff between artifact reduction and temporal fidelity. (B) A line profile was drawn through the heart. (C) Plots of the line profile over all cardiac phases are shown. For small values of λ_2, the profiles appear noisy but have good temporal fidelity. Temporal blurring is observed when λ_2 is too large (λ_2=0.05). A value of λ_2=0.01 reduces noise and artifacts while preserving the temporal dynamics.

Figure 4. *Image registration and pattern matching.* The leftmost panel shows reconstructed subspace images corresponding to the first three singular values (K=1 through K=3) for three cardiac phases. Phase 1 is in systole, while phases 2 and 3 are in diastole. Next, non-rigid deformation fields are used to register the images to the same phase. In this example, phase 3 is selected as the target phase. The registered images are then averaged over the cardiac phase dimension and matched to the dictionary to generate T_1 and T_2 maps. Additionally, the image corresponding to the second singular value (highlighted in orange) is used as a cine frame. Image registration and pattern matching are repeated, each time registering the reconstructed subspace images to a different cardiac phase to generate maps and cine images throughout the cardiac cycle.

Figure 5. *Simulation results under conditions of constant ground truth T_1 and T_2.* (A) T_1 and T_2 maps are shown for representative diastolic and systolic frames. Results are shown for (top left) the ground truth, (top right) low-rank reconstruction with no motion binning, (bottom left) low-rank reconstruction using 24 cardiac phases, and (bottom right) low-rank reconstruction with 24 cardiac phases followed by non-rigid registration. Measures of accuracy (relative percent error

in myocardial T_1 and T_2) and precision (coefficient of variation) are reported. (B) Image sharpness (i.e. apparent myocardial wall thickness) is plotted for each technique.

Figure 6. *Simulation results under conditions with variable ground truth T_1 and T_2 throughout the cardiac cycle.* (A) The ground truth T_1 increased from 1340ms in diastole to 1400ms in systole, (B) while the ground truth T_2 decreased from 50ms in diastole to 44ms in systole. The ground truth values are plotted in black, the low-rank reconstruction with 24 cardiac phases is plotted in blue, and the low-rank reconstruction with 24 phases and non-rigid registration is plotted in red.

Figure 7. *Cine-MRF results using the ISMRM/NIST MRI system phantom at 3T.* (A) Phantom T_1 and T_2 times are compared across cardiac phases. (B) Linear regression comparing reference values with relaxation times measured using cine-MRF averaged over all phases. The identity line is plotted in black, and the best-fit line and Pearson's correlation are reported. (C) Bland-Altman plots comparing reference values with relaxation times measured using cine-MRF averaged over all phases. For T_1, the bias is 4.6ms and 95% limits of agreement are (-29.8, 39.0)ms. For T_2, the bias is -1.5ms and 95% limits of agreement are (-11.1, 8.2)ms.

Figure 8. *Comparison of cine-MRF, ECG-triggered cardiac MRF, and conventional scans in a subject at 3T*. (A) Examples of cine-MRF T_1 and T_2 maps in diastole and systole are shown. For comparison, maps were also collected with ECG-triggered cMRF, MOLLI, and T_2-prepared FLASH. The ECG-triggered scans were repeated twice with the scan window placed once in diastole and once in systole. (B) Examples of cine images derived from the cine-MRF scan (left) compared to a conventional cine (right). Although cine-MRF uses a FISP-based readout with variable sequence parameters and the conventional cine uses a bSSFP readout, the image

contrast in both datasets is quite similar with blood appearing bright and myocardium appearing dark.

Figure 9. *Relaxation times measured in each medial myocardial segment in healthy subjects at 3T.* The mean (A) T_1 and (B) T_2 values measured in different myocardial segments at a medial slice are presented for cine-MRF, ECG-triggered cMRF, and MyoMaps (MOLLI for T_1 mapping and T_2-prepared FLASH for T_2 mapping). Results are shown for diastolic and systolic phases. The error bars indicate the standard deviation across subjects.

Figure 10. *Bland-Altman plots comparing diastolic myocardial T_1/T_2 values.* These plots compare the mean T_1 and T_2 values measured in diastole with cine-MRF, ECG-triggered cMRF, and conventional mapping sequences (MOLLI for T_1 mapping and T_2-prepared FLASH for T_2 mapping). The solid red lines depict the mean bias between any two methods. The dotted red lines show the 95% limits of agreement.

Figure 11. *Bland-Altman plots comparing systolic myocardial T_1/T_2 values.* These plots compare the mean T_1 and T_2 values measured in systole with cine-MRF, ECG-triggered cMRF, and conventional mapping sequences (MOLLI for T_1 mapping and T_2-prepared FLASH for T_2 mapping). The solid red lines depict the mean bias between any two methods. The dotted red lines show the 95% limits of agreement.

Figure 12. *Intrasubject and intersubject variation for the in vivo study*. (A) Intrasubject variation, as quantified by the coefficient of variation (CV), are shown for each method in diastole and systole. (B) Intersubject variation for each method in diastole and systole are shown, as measured by the CV.

Figure 13. *Cine images using cine-MRF and a standard balanced SSFP acquisition.* Cine frames during diastole and systole are shown for apical, medial, and basal slice positions acquired with (A) cine-MRF and (B) a standard bSSFP cine scan. The measured LV ejection fraction was 55.5% for cine-MRF and 54.0% for the standard cine.

Figure 14*. Bland-Altman plots comparing measures of LV function between cine-MRF and a standard bSSFP cine scan*. Results are shown for (A) end-diastolic volume, (B) end-systolic volume, and (C) ejection fraction over the entire left ventricle for data collected from six healthy subjects. (D) Additionally, results are shown for single-slice ejection fraction measured at a medial slice position for data collected in 17 healthy subjects. The solid red lines indicate the mean bias, and the dotted red lines indicate the 95% limits of agreement.

Additional Files

Additional File 1. This file provides the schedule of flip angles, inversion times, and T_2 preparation times for the cine-MRF sequence.

Additional File 2. This file contains a figure showing results from the intrareader repeatability study.

Supporting Video 1. This movie shows T_1 maps, T_2 maps, and contrast-weighted cine images from a cine-MRF scan in a healthy subject at 3T.

Supporting Video 2. This movie shows T_1 maps, T_2 maps, and contrast-weighted cine images from a cine-MRF scan in a healthy subject at 3T.

Supporting Video 3. This movie shows T_1 maps, T_2 maps, and contrast-weighted cine images from a cine-MRF scan in a healthy subject at 3T.

Supporting Video 4. This movie shows T_1 maps, T_2 maps, and contrast-weighted cine images from a cine-MRF scan in a healthy subject at 3T.

Supporting Video 5. This movie compares contrast-weighted cine images from cine-MRF (left panel) and a standard bSSFP cine scan (right panel) at multiple slices covering the left ventricle.

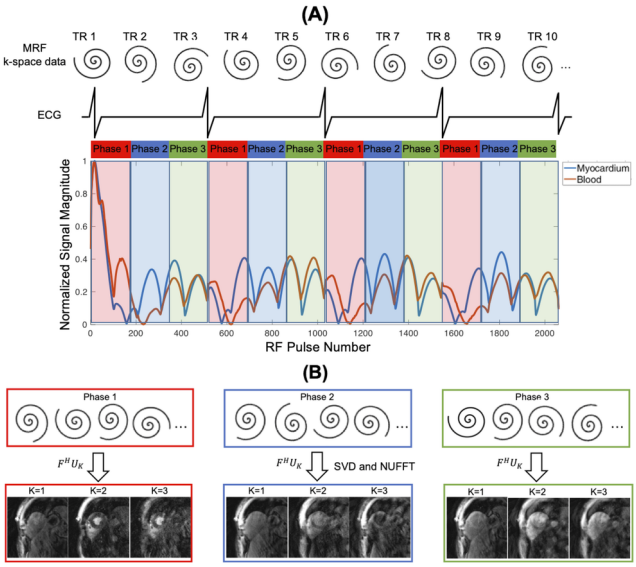

NBM_4323_Figure1.tif

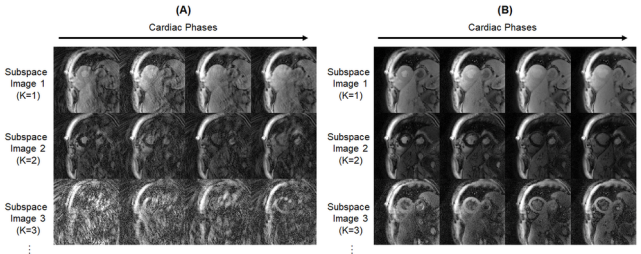

NBM_4323_Figure2.tif

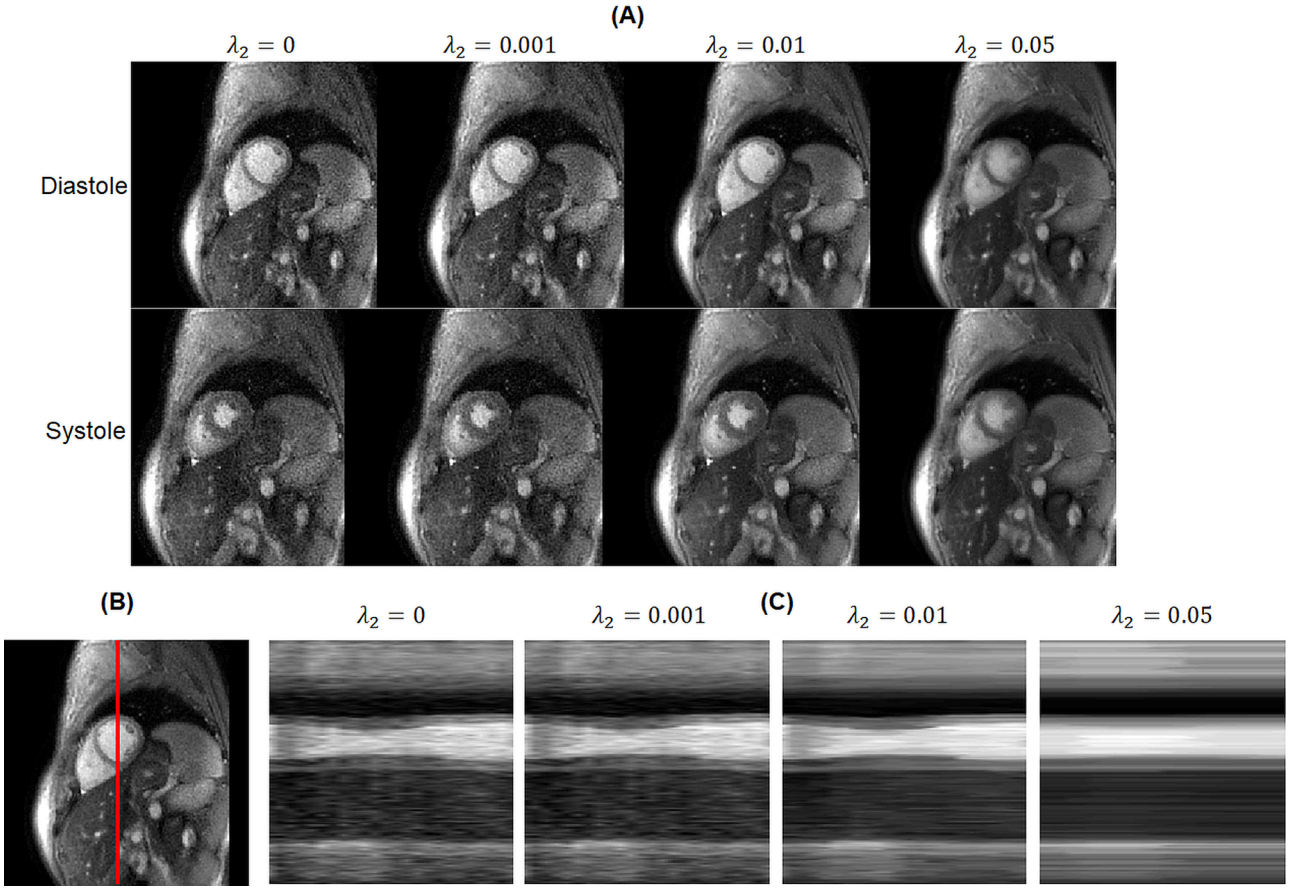

NBM_4323_Figure3.tif

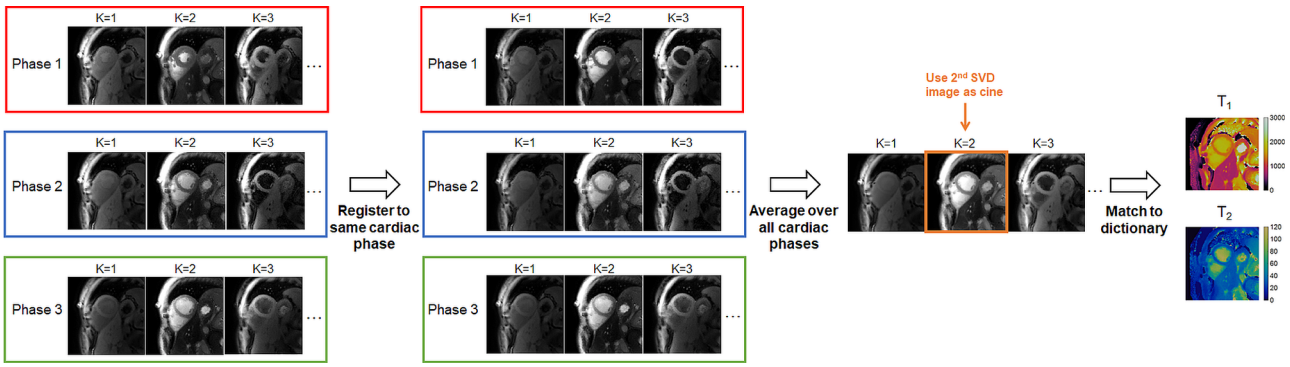

NBM_4323_Figure4.tif

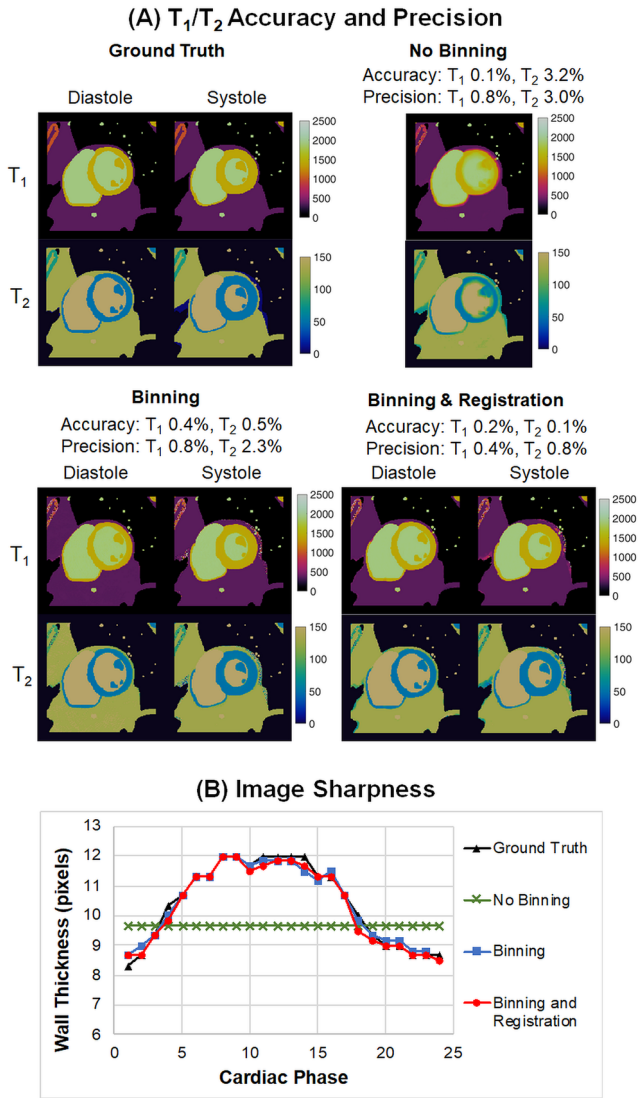

NBM_4323_Figure5.tif

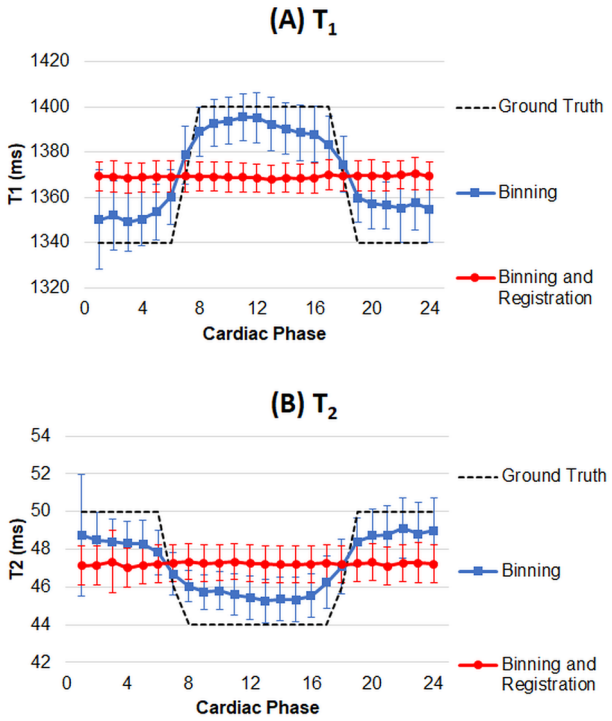

NBM_4323_Figure6.tif

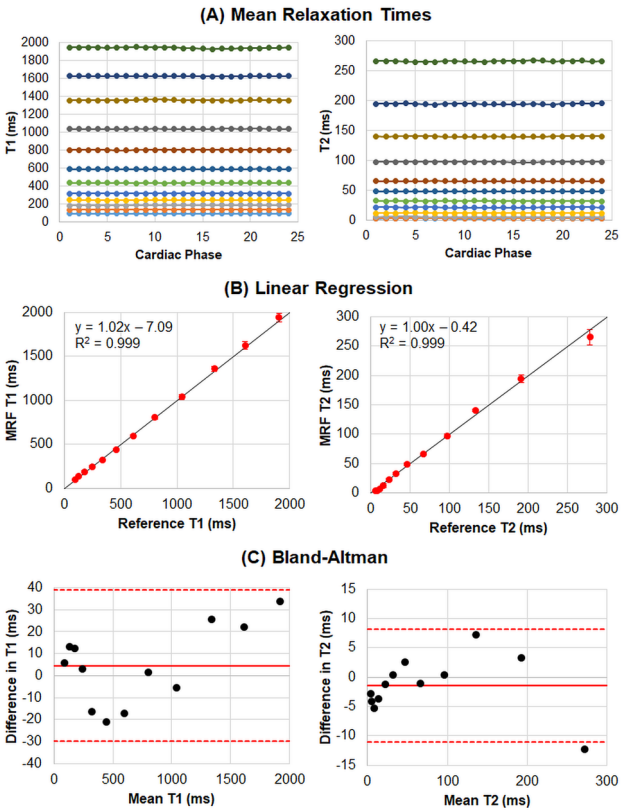

NBM_4323_Figure7.tif

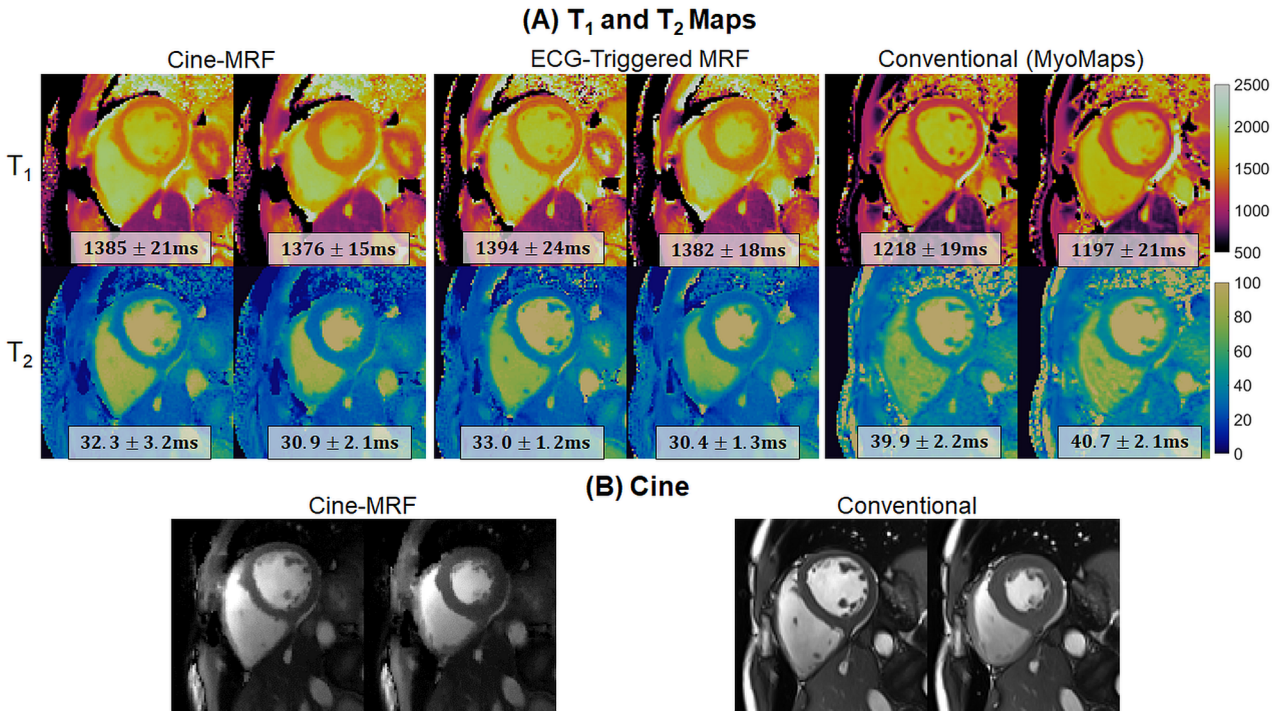

NBM_4323_Figure8.tif

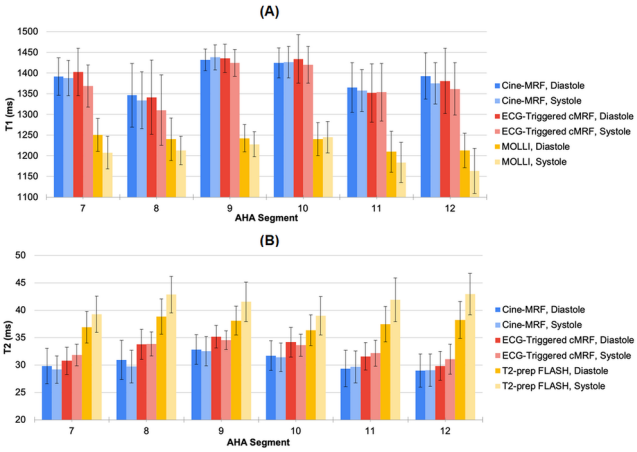

NBM_4323_Figure9.tif

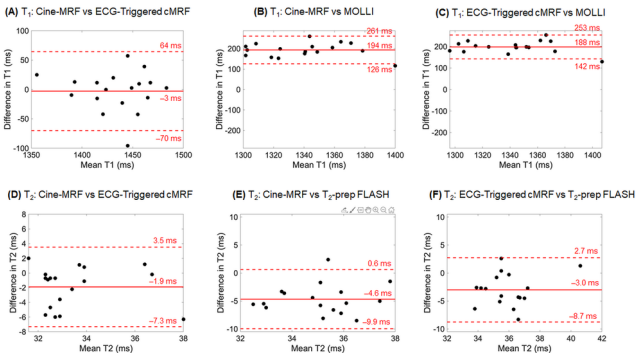

NBM_4323_Figure10.tif

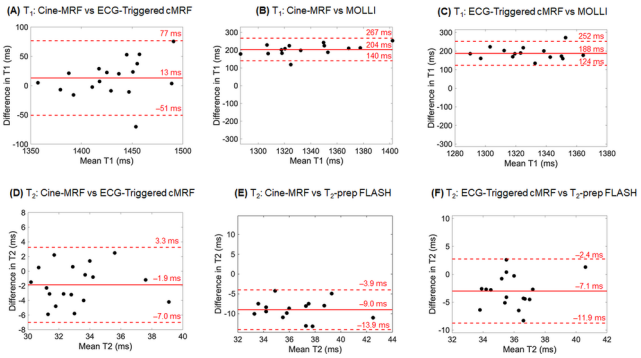

NBM_4323_Figure11.tif

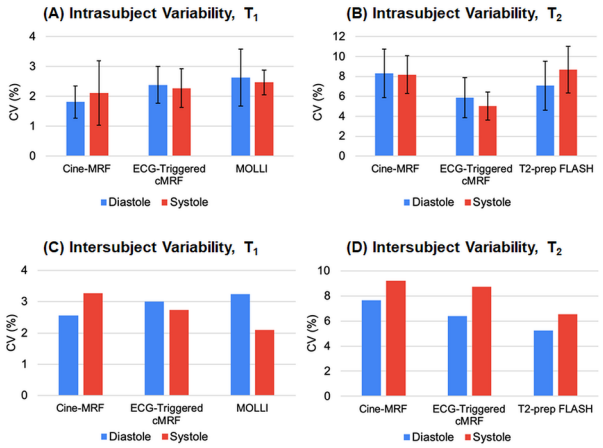

NBM_4323_Figure12.tif

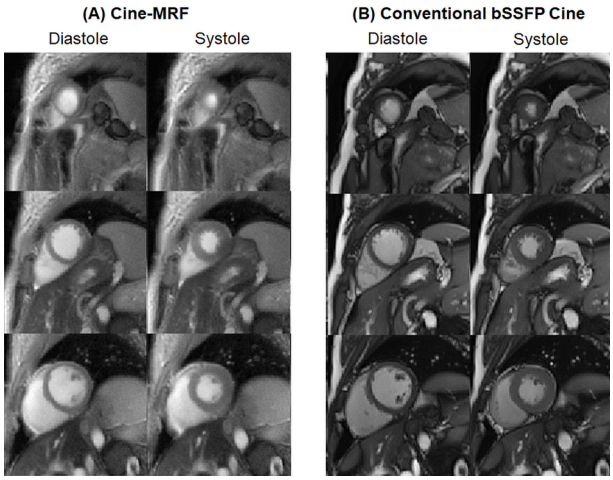

NBM_4323_Figure13.tif

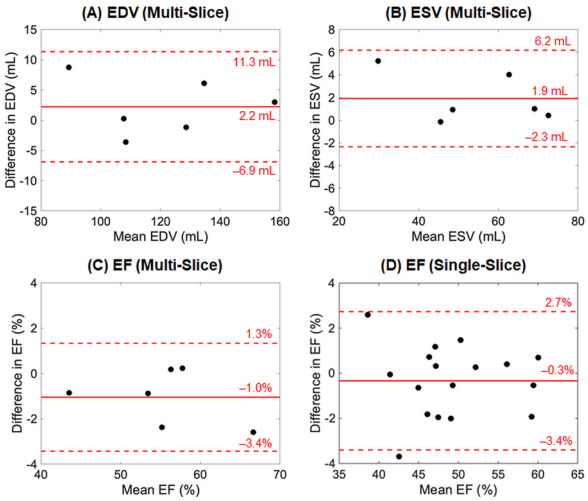

NBM_4323_Figure14.tif